ACCSCIENCE PUBLISHING

International Journal of Bioprinting

RESEARCH ARTICLE

CGA–Eu nanozyme-functionalized 3D-printed scaffolds accelerate osteoporotic bone regeneration via ROS scavenging and angio-osteogenic modulation

Wenjie Zhao[1,2†], Xinyu Ding[1†], Shuai Chen[1†], Jiachen Zhang[1], Yuqing Zhou[1], Miaochao Qin[1], Peng Ma[1], Pengfei Sun[1], Hao Chen[1*], Wen Min[1*], and Junwu Wang[1*]

[1]Department of Orthopedics, Affiliated Hospital of Nanjing University of Chinese Medicine, Nanjing, Jiangsu, China

[2]Department of Orthopedics, Northern Jiangsu People's Hospital, Nanjing University, Yangzhou, Jiangsu, China

[†]*These authors contributed equally to this work.*

***Corresponding authors:**
Junwu Wang
(wjw818@njucm.edu.cn)
Wen Min
(wmin@njucm.edu.cn)
Hao Chen
(261024@njucm.edu.cn)

Citation: Zhao W, Ding X, Chen S, *et al*. CGA–Eu nanozyme-functionalized 3D-printed scaffolds accelerate osteoporotic bone regeneration via ROS scavenging and angio-osteogenic modulation. *Int J Bioprint*. 2026;12(3):026130117. doi: 10.36922/IJB026130117

Received: March 26, 2026

Revised: May 5, 2026

Accepted: May 7, 2026

Published online: May 7, 2026

Abstract

Impaired bone regeneration in osteoporosis primarily stems from a local pathological microenvironment characterized by high levels of reactive oxygen species (ROS), which severely inhibits osteogenic differentiation and angiogenesis. To address this challenge, this study engineered a 3D-printed multifunctional composite scaffold consisting of an α-tricalcium phosphate/zinc oxide (α-TCP/ZnO) matrix loaded with chlorogenic acid–europium (CGA–Eu) metal-phenolic network nanoparticles. The incorporation of ZnO effectively buffered the acidity generated by α-TCP degradation, thereby maintaining a physiological pH environment favorable for regeneration. Furthermore, CGA–Eu endowed the scaffold with potent antioxidant capacity, enabling it to efficiently scavenge excessive ROS and significantly alleviate oxidative damage *in vitro*. Biological evaluations confirmed that the sustained release of Eu^{3+}, Zn^{2+}, and CGA cooperatively promoted osteogenic differentiation of bone marrow mesenchymal stem cells and angiogenic activity in human umbilical vein endothelial cells. In an ovariectomized rat cranial defect model, the composite scaffold effectively accelerated bone mass accumulation and enhanced angiogenesis. In conclusion, this dual microenvironment-regulating strategy, which integrates pH buffering, ROS scavenging, and sustained osteo-angiogenic ion delivery, offers a promising scaffold design for osteoporotic bone defect repair.

Keywords: 3D bioprinting; Bone regeneration; Chlorogenic acid; Europium; Microenvironment remodeling

1. Introduction

The repair of osteoporotic bone defects remains a severe clinical challenge, primarily because the complex local pathological microenvironment severely impairs the regenerative capacity of bone tissue. Although systemic bone loss is a hallmark of osteoporosis, the abnormal accumulation of reactive oxygen species (ROS) at the defect

site constitutes a critical pathological factor hindering bone tissue repair.[1,2] High levels of oxidative stress induce premature senescence and dysfunction in bone marrow mesenchymal stem cells (BMSCs) and vascular endothelial cells, thereby inhibiting osteogenic differentiation and microvascular network reconstruction, ultimately leading to impaired bone healing.[3-5] Consequently, traditional inorganic scaffolds, which merely provide structural support and lack the capability to actively scavenge ROS and remodel a pro-regenerative microenvironment, often fail to achieve satisfactory repair outcomes under osteoporotic conditions.[6]

Inorganic materials, particularly calcium phosphates, have been widely used in bone tissue engineering due to their high similarity to the mineral composition of natural bone.[7,8] However, single-phase β-tricalcium phosphate (β-TCP) or α-tricalcium phosphate (α-TCP) often lack the sufficient bioactivity required to effectively promote bone repair in osteoporotic patients.[9-12] Traditionally, β-TCP requires high-temperature sintering, which limits bioactive loading to surface coatings that typically show burst release and poor long-term integration.[12,13] In contrast, α-TCP exhibits faster biodegradation and a unique room-temperature hydration capacity.[14] This self-setting reaction produces a brushite network with suitable rheological properties for 3D bioprinting, enabling the stable incorporation of bioactive molecules into the matrix.[9,10,15] Nevertheless, the acidic byproducts released during early brushite degradation create a localized low-pH environment that is unfavorable for bone tissue regeneration.[9,16] To address this issue, we used zinc oxide (ZnO) nanoparticles. The slightly alkaline ZnO nanoparticles effectively neutralize the acidic byproducts generated by α-TCP degradation, simultaneously endowing the scaffold with antioxidant properties.[17,18] Furthermore, the Zn^{2+} released during degradation serves as an essential cofactor for alkaline phosphatase (ALP), directly enhancing enzyme activity and promoting mineral deposition.[17,19] Mechanistically, Zn^{2+} upregulates the expression of key markers, including the core osteogenic transcription factor Runt-related transcription factor 2 (RUNX2), type I collagen (Col-I), and osteocalcin (OCN), by activating intracellular signaling cascades such as cyclic adenosine monophosphate (cAMP)/protein kinase A (PKA).[20,21] Nevertheless, in the complex pathological context of osteoporosis, the metabolic support provided solely by Zn^{2+} release from inorganic scaffolds still lacks the regulatory capacity to actively intervene in the local pathological microenvironment.

To overcome the limited active regulation of inorganic scaffolds, a metal-phenolic network (MPN) driven by the coordination of chlorogenic acid (CGA) and europium ions (Eu^{3+}) was constructed and integrated into the scaffold matrix. As a natural polyphenol, CGA contains abundant phenolic hydroxyl groups that can efficiently scavenge free radicals, significantly alleviating cellular oxidative stress.[22] However, the chemical instability and burst release of free CGA limit its long-term biological effects.[23,24] To address this, we constructed stable CGA–Eu nanoparticles driven by the coordination of Eu^{3+} with CGA, synergized by intermolecular electrostatic and hydrophobic effects. This structure not only improves the stability of CGA but also enables pH- and ROS-responsive release.[25-27] In the mildly acidic and oxidative microenvironment of osteoporotic defects, the coordination bonds gradually dissociate, allowing for the continuous and on-demand delivery of bioactive components. Beyond serving as a structural stabilizer, the released Eu^{3+} acts as a potent bioactive ion that plays multiple roles in both osteogenesis and angiogenesis.[28,29] Eu^{3+} promotes the proliferation and spreading of endothelial cells and stimulates the secretion of vascular endothelial growth factor (VEGF) and matrix metalloproteinase-9 (MMP-9), accelerating the early reconstruction of local microvascular networks.[30,31] Furthermore, it upregulates key osteogenic factors, such as ALP and osteopontin (OPN), to promote bone matrix mineralization.[31]

In osteoporotic bone defects, osteogenic and angiogenic capacity is compromised, and the adverse microenvironment, particularly oxidative stress, further impairs cell function. To address this, we designed an α-TCP/ZnO/CGA-Eu composite scaffold that integrates structural support with microenvironmental remodeling to promote osteogenesis and angiogenesis, thereby overcoming the inherent limitations of conventional inorganic materials (Figure 1). Specifically, ZnO neutralizes the acidic byproducts of α-TCP degradation and releases osteogenic Zn^{2+}, while the CGA–Eu scavenges excess ROS through responsive release and provides sustained Eu^{3+} delivery, synergistically enhancing osteogenesis and angiogenesis. *In vitro* evaluations confirmed that the scaffold scavenged ROS, thereby promoting the osteogenic differentiation of BMSCs and the angiogenic activity of human umbilical vein endothelial cells (HUVECs). *In vivo*, using an ovariectomized (OVX) rat cranial defect model, we demonstrated that the scaffold accelerated local bone mass accumulation and vascular network reconstruction under osteoporotic conditions. This composite system, integrating physical support, microenvironment remodeling, and coupled osteo-angiogenic promotion, holds great promise as a therapeutic strategy for osteoporotic bone defects.

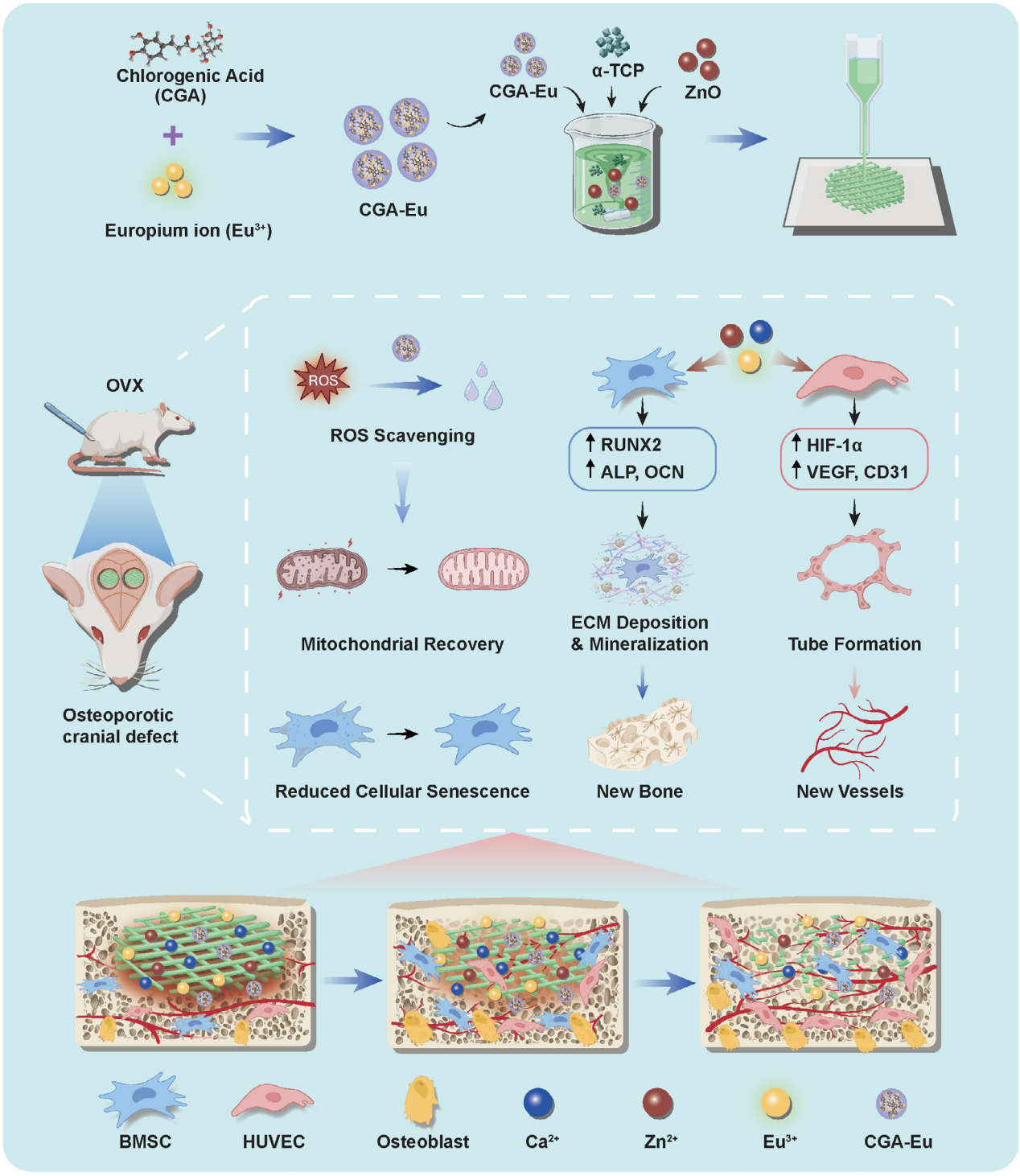

Figure 1. Schematic illustration of the preparation of α-tricalcium phosphate/zinc oxide/chlorogenic acid–europium (α-TCP/ZnO/CGA–Eu) scaffold and its treatment for osteoporotic bone defects. Image created with Biorender.com. Zhao W. (2026) https://BioRender.com/97hjvn4

Abbreviations: ALP: Alkaline phosphatase; BMSC: Bone marrow mesenchymal stem cell; ECM: Extracellular matrix; HIF-1α: Hypoxia-inducible factor 1-alpha; HUVEC: Human umbilical vein endothelial cell; OCN: Osteocalcin; OVX: Ovariectomized; ROS: Reactive oxygen species; RUNX2: Runt-related transcription factor 2; VEGF: Vascular endothelial growth factor.

2. Materials and methods

2.1. Materials

Sodium alginate (Alg), α-TCP, CGA, europium nitrate hexahydrate ($Eu(NO_3)_3 \cdot 6H_2O$), and ZnO were purchased from Sigma-Aldrich (United States of America [USA]). 2,2-Diphenyl-1-picrylhydrazyl (DPPH) and 2,2'-azino-bis (3-ethylbenzothiazoline-6-sulfonic acid) (ABTS) radical scavenging assay kits, as well as that of fluorescein isothiocyanate (FITC)–phalloidin, were purchased from Solarbio (China). Cell culture reagents, including α-minimum essential medium (α-MEM), endothelial cell basal medium, fetal bovine serum (FBS), and penicillin/streptomycin (P/S), were purchased from Gibco (USA). Cell Counting Kit-8 (CCK-8), lactate dehydrogenase (LDH) cytotoxicity assay kit, 5-ethynyl-2'-deoxyuridine (EdU) cell proliferation assay kit, dihydroethidium (DHE) ROS fluorescent probe, tetramethylrhodamine ethyl ester perchlorate (TMRE) assay kit, Hoechst 33342, 4',6-diamidino-2-phenylindole (DAPI), senescence-associated β-galactosidase (SA-β-gal) staining kit, ALP staining kit, Alizarin red S (ARS) staining kit, and Von Kossa staining kit were all purchased from Beyotime Biotechnology (China). Matrigel was purchased from Corning (USA). Hematoxylin and eosin (H&E) staining kits, Masson's trichrome staining kits, and immunohistochemistry (IHC) kits were purchased from Servicebio (China). The total RNA extraction kit, reverse transcription kit, and SYBR Green qPCR Master Mix were purchased from Thermo Fisher Scientific (USA). Primary antibodies against RUNX2, ALP, OCN, platelet endothelial cell adhesion molecule-1 (PECAM-1/CD31), VEGF, and hypoxia-inducible factor 1-alpha (HIF-1α), along with the corresponding fluorophore-conjugated secondary antibodies, were purchased from Proteintech (China).

2.2. Preparation and characterization of chlorogenic acid–europium nanoparticles

The synthesis procedure of CGA–Eu nanoparticles is illustrated in Figure 2A. Briefly, CGA was dissolved in deionized water to form a homogeneous solution. Under continuous magnetic stirring (500 rpm) at room temperature, the $Eu(NO_3)_3 \cdot 6H_2O$ solution was added dropwise into the mixture at a constant rate. Subsequently, the pH of the mixture was slowly adjusted to 6.5–7.5 using 1 M NaOH solution to promote the deprotonation of the phenolic hydroxyl groups of CGA and their coordination-driven self-assembly with Eu^{3+}. After continuous stirring for 2 h, the resulting CGA–Eu nanoparticles were collected by centrifugation at 10,000 rpm for 10 min, washed three times with deionized water to remove unreacted precursors, and finally resuspended and lyophilized in a freeze-dryer for further use.

The micromorphology of the nanoparticles was observed using a scanning electron microscope (SEM; ZEISS Sigma 500, Carl Zeiss Microscopy GmbH, Germany) and a transmission electron microscope (TEM; FEI Tecnai G2 F20, Thermo Fisher Scientific, USA). The hydrodynamic size distribution of the particles was analyzed via dynamic light scattering (DLS). The *in vitro* antioxidant capacity of the CGA–Eu nanoparticles was evaluated through DPPH and ABTS radical scavenging assays. Sample suspensions of CGA–Eu nanoparticles at various concentrations (or an equal volume of deionized water as a control) were added to the corresponding working solutions and incubated for 30 min at room temperature in the dark. Subsequently, the supernatant was collected, and the optical density (OD) at 515 nm (DPPH) and 734 nm (ABTS) was measured using a multimode microplate reader (VICTOR Nivo, PerkinElmer, USA). The radical scavenging rate was calculated using the following formula:

$$\text{Scavenging rate}(\%) = \frac{A_c - A_s}{A_c} \times 100\% \quad (1)$$

where A_s is the absorbance of the sample group, and A_c is the absorbance of the control group.

2.3. Preparation of 3D-printed scaffolds

The composite scaffolds were constructed using an extrusion-based 3D bioprinter (SunP BioMaker 2, SunP Biotech, USA). The ink formulation and printing parameters were adopted from our previously validated α-TCP-based scaffold system.[14,15] To prepare the ink, α-TCP powder (3 g), ZnO (2% w/v), and CGA–Eu nanoparticles (5% w/v) were sequentially and slowly added into a 10% (w/v) Alg gel solution. Similarly, the printing parameters were selected within a workable printing window to maintain continuous extrusion and shape fidelity: a nozzle diameter of 500 μm, extrusion rate of 0.5–1 mm^3/s, and printing speed of 5–15 mm/s. The scaffolds were printed as layer-cross-deposited grid-like constructs. For *in vitro* experiments, rectangular scaffolds with dimensions of 10 mm × 10 mm × 5 mm were prepared. For the OVX rat cranial defect model, cylindrical scaffolds with a diameter of 5 mm and a thickness of 1 mm were fabricated to match the 5-mm critical-sized cranial defects. The deposited scaffold struts were relatively dense, whereas the interconnected macroporous architecture was generated by the regular square openings between adjacent struts. The designed inter-strut macropore size was approximately 300 μm × 300 μm. After printing, the formed scaffolds were immediately immersed in a 5% (w/v) $CaCl_2$ solution to achieve sufficient cross-linking

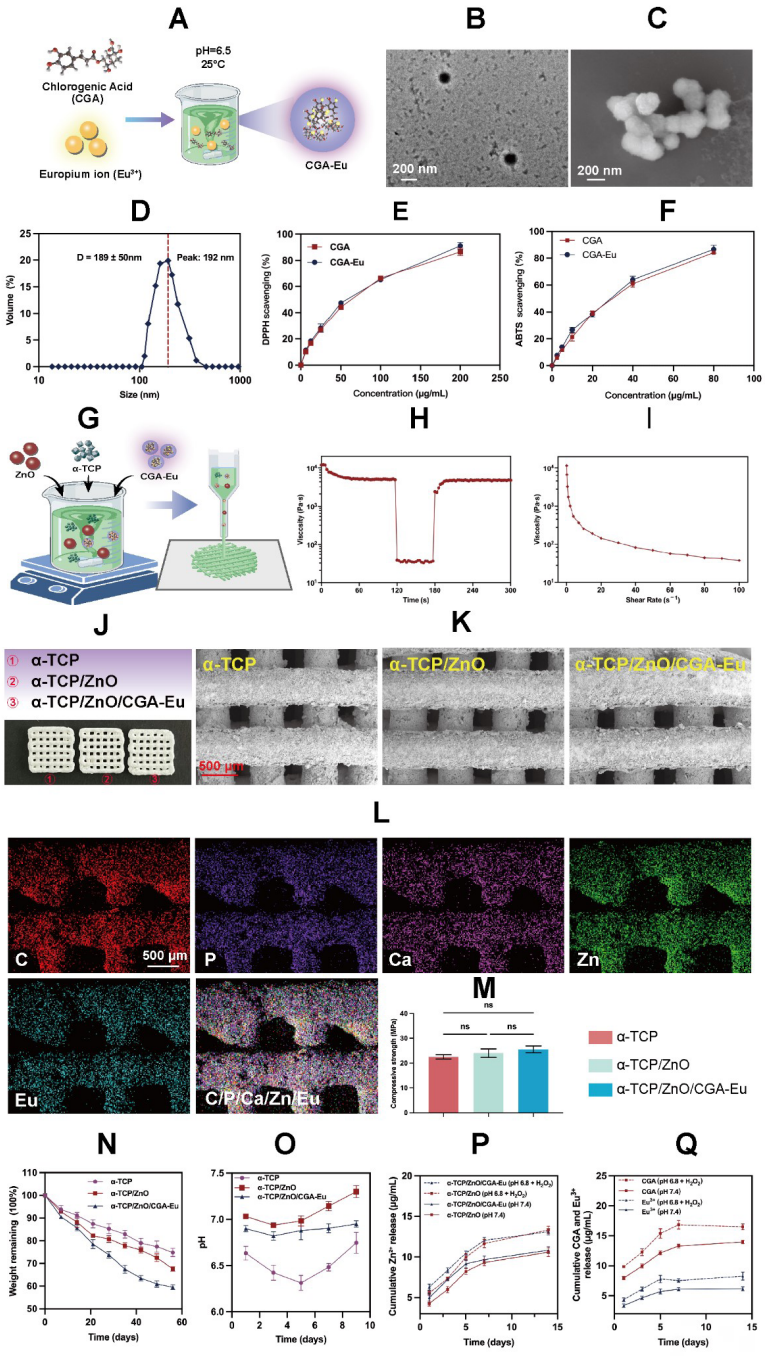

Figure 2. Synthesis and characterization of CGA–Eu nanoparticles and composite scaffolds. (A) Synthesis schematic of CGA–Eu. (B) Transmission electron microscopy and (C) scanning electron microscopy (SEM) images of CGA–Eu. Scale bars: 200 nm; magnifications: 60,000×. (D) Size distribution of CGA–Eu measured by dynamic light scattering. (E) DPPH and (F) ABTS radical scavenging activities of CGA–Eu. (G) 3D printing process of composite scaffolds. (H, I) Rheological testing of the bioink. (J) Macroscopic morphology, (K) SEM microstructure (scale bars: 500 μm; magnifications: 45×), and (L) energy-dispersive X-ray spectrometer (scale bars: 500 μm; magnifications: 50×) mapping of the scaffold. (M) Compressive strength of the scaffolds. (N) *In vitro* degradation and (O) corresponding pH variation. Cumulative release profiles of (P) Zn^{2+} and (Q) CGA and Eu^{3+} under physiological (pH 7.4) and simulated osteoporotic (pH 6.8 + 100 μmol H_2O_2) conditions. Notes: ns: No significance. $n = 3$.

Abbreviations: α-TCP: α-tricalcium phosphate; ABTS: 2,2'-azino-bis (3-ethylbenzothiazoline-6-sulfonic acid); CGA–Eu: Chlorogenic acid–europium; DPPH: 2,2-Diphenyl-1-picrylhydrazyl; ZnO: Zinc oxide.

and solidification. Subsequently, the scaffolds were washed three times with deionized water to remove excess calcium ions, rapidly vacuum-dried, and stored in a desiccator for further use.

2.4. Physicochemical characterization of scaffolds

The rheological properties of the bioinks were evaluated at 25 °C using a Kinexus Pro rheometer (Malvern, United Kingdom). After printing, the macroscopic morphology of the scaffolds was recorded with a digital camera (Nikon Z50, Nikon Corporation, Japan). Subsequently, an SEM equipped with an energy-dispersive X-ray spectrometer (EDS; Oxford X-Max 80 detector, Oxford Instruments, United Kingdom) was utilized to observe the microscopic pore structure and surface morphology of the scaffolds in each group, as well as to analyze the distribution of core elements (C, P, Ca, Zn, and Eu).

To evaluate scaffold degradation and pH variations, the weighed scaffolds were immersed in PBS (pH 7.4) at a mass-to-volume ratio of 0.2 g/mL and incubated in a constant-temperature shaker at 37 °C and 100 rpm. Meanwhile, to investigate the stimuli-responsive release behavior of the scaffolds, a simulated osteoporotic microenvironment (PBS at pH 6.8 containing 100 μM H_2O_2) was employed as the releasing medium.[32,33] The pH of the PBS was measured every two days using a pH meter (PHS-25, LeiCi, China), and the PBS was then replaced with fresh PBS. At predetermined time points from week 1 to week 8, the scaffolds were retrieved, gently washed with deionized water, dried, and weighed to determine the residual mass. The residual weight percentage was calculated using the following formula:

$$\text{Residual weight}(\%) = \frac{W_t}{W_0} \times 100\% \quad (2)$$

where W_t is the dry weight at a specific time point, and W_0 is the initial dry weight. The collected PBS replacement solutions were used to determine the concentrations of Zn^{2+} and Eu^{3+} via inductively coupled plasma optical emission spectrometry (ICP-OES, Prodigy 7, Leeman Labs Inc., USA), while the release of CGA was quantified using UV–Vis spectrophotometry. Finally, the compressive strength of the scaffolds was tested using an electronic universal testing machine (Exceed 40, MTS, USA).

2.5. Cell culture and *in vitro* biocompatibility evaluation

Bone marrow mesenchymal stem cells were isolated from the bone marrow of the femurs and tibias of 4-week-old Sprague-Dawley (SD) rats, and cultured in α-MEM supplemented with 10% FBS and 1% P/S. HUVECs were cultured in an endothelial cell basal medium containing specific growth factors. All cells were incubated in a humidified incubator at 37 °C with 5% CO_2. The culture medium was replaced every 2 days, and cells at passage 3 were used for subsequent experiments.

To evaluate biocompatibility, the scaffolds of each group were immersed in complete culture medium at a mass-to-volume ratio of 0.2 g/mL and incubated at 37 °C for 72 h. The scaffolds were then removed, and the scaffold extracts were collected and sterilized using a 0.22 μm filter membrane. BMSCs were seeded into 96-well plates at a density of 5×10^3 cells/well. After overnight cell attachment, the medium was replaced with the scaffold extracts of each group containing 10% FBS. On days 1, 3, and 5, CCK-8 working solution was added and incubated for 1 h. The OD at 450 nm was measured using a microplate reader to evaluate cell proliferation and viability. To assess early cytotoxicity, the culture supernatant on day 3 was collected, and the LDH release was measured using an LDH assay kit according to the manufacturer's instructions, with absorbance read at 490 nm. For cytoskeleton observation, BMSCs cultured in the extracts for 3 days were fixed with 4% paraformaldehyde. After permeabilization with 0.1% Triton X-100, the cytoskeleton (F-actin) and nuclei were fluorescently stained with FITC–phalloidin and DAPI, respectively. The area of the BMSCs was quantitatively analyzed using ImageJ software (1.54 g, National Institutes of Health, USA). Additionally, cell proliferation was evaluated using an EdU assay kit. After labeling the cells with EdU for 2 h, the nuclei were counterstained with Hoechst 33342. The percentage of EdU-positive cells was observed and quantified under a fluorescence microscope (ZEISS Axio Imager 2, Carl Zeiss Microscopy GmbH, Germany).

2.6. *In vitro* antioxidative stress evaluation

To evaluate the antioxidant capacity of each scaffold at the cellular level, H_2O_2 was used to induce oxidative stress, followed by treatment with extracts from each group. Intracellular ROS were labeled using a DHE fluorescent probe. Fluorescence microscopy images were captured, and the relative fluorescence intensity of DHE was quantitatively analyzed using ImageJ software. Similarly, the mitochondrial membrane potential was assessed using a TMRE assay kit. Cells were incubated with TMRE staining solution at 37 °C for 20 min in the dark. After washing with PBS, the red fluorescence signals of TMRE were captured using a fluorescence microscope, and the relative fluorescence intensity was quantified via ImageJ software.

2.7. Effects of different scaffolds on osteogenic differentiation

To simulate the local oxidative stress pathological microenvironment of osteoporosis, H_2O_2 was added to the BMSCs culture medium to induce a high ROS state. An SA-β-gal staining kit was used according to the manufacturer's instructions to evaluate the rescue effect of the scaffold extracts from each group on H_2O_2-induced cellular senescence.

For the osteogenic differentiation assay, BMSCs were seeded into 24-well plates at a density of 2×10^4 cells/well. Upon reaching 80% confluence, the medium was replaced with osteogenic induction medium (supplemented with 50 μg/mL ascorbic acid, 10 mM β-glycerophosphate sodium, and 10 nM dexamethasone) containing the respective scaffold extracts. The culture medium was refreshed every three days. After 7 days of induction, the cells were fixed with 4% paraformaldehyde for 15 min and observed colorimetrically using an ALP staining kit. On day 21 of induction, a 1% ARS solution and a Von Kossa staining kit were employed to evaluate the deposition of calcium nodules and the extent of extracellular matrix mineralization, respectively. The mineralized area was quantitatively analyzed using ImageJ software.

On day 7 of induction, the cells were lysed to extract total RNA using a total RNA extraction kit, and the RNA was subsequently reverse-transcribed into cDNA. Amplification was performed on a real-time quantitative polymerase chain reaction (PCR) instrument (Applied Biosystems 7500, Applied Biosystems, USA) using SYBR Green Master Mix to analyze the relative mRNA expression levels of osteogenesis-related genes (*Runx2*, *Alp*, and *Ocn*) (primer sequences are listed in Table 1), with *GAPDH* serving as the internal control.

Immunofluorescence staining was performed as follows: after fixation with 4% paraformaldehyde, permeabilization with 0.1% Triton X-100, and blocking with 1% bovine serum albumin (BSA), the cells were incubated overnight at 4 °C with primary antibodies against RUNX2 and OCN. Following thorough washing, the cells were incubated with the corresponding fluorophore-conjugated secondary antibodies for 1 h at room temperature in the dark. The nuclei were counterstained with DAPI, and images were acquired using a fluorescence microscope.

2.8. Effects of different scaffolds on angiogenesis

To investigate the pro-angiogenic effects of the composite scaffolds under oxidative stress, HUVECs were first subjected to H_2O_2-induced oxidative stress. Cell proliferation following treatment with the respective scaffold extracts was evaluated using an EdU assay kit as described in Section 2.5, and the proportion of EdU-positive cells was quantified.

The ability of HUVECs to form capillary-like structures was evaluated via a tube formation assay. Pre-chilled Matrigel was evenly coated onto the bottom of a 24-well plate and allowed to solidify at 37 °C for 30 min. Serum-starved HUVECs were resuspended in media containing different scaffold extracts at a density of 2×10^4 cells/well and seeded onto the Matrigel. After incubation for 6–8 h, the formation of capillary-like networks was observed under a microscope (ZEISS Axio Observer 5, Carl Zeiss Microscopy GmbH, Germany), and the total tube length was quantitatively analyzed using ImageJ software equipped with the Angiogenesis Analyzer plugin.

The expression of angiogenesis-related genes (*VEGF*, *CD31*, and *HIF1A*) was detected via quantitative reverse transcription PCR (qRT-PCR). The primer sequences are listed in Table 2. After three days of culturing in the extracts under oxidative stress, HUVECs were collected for total RNA extraction. The remaining qRT-PCR steps were consistent with those described in Section 2.7. The expression of CD31 and VEGF in each group was

Table 1. Primer sequences used for qRT-PCR analysis of BMSC osteogenesis

Genes	Species	Forward primer	Reverse primer
Gapdh	Rat	AGACAGCCGCATCTTCTTGT	CTTGCCGTGGGTAGAGTCAT
Runx2	Rat	ACTTCCTGTGCTCGGTGCT	GACGGTTATGGTCAAGGTGAA
Alp	Rat	AACGTGGCCAAGAACATCATCA	TGTCCATCTCCAGCCGTGTC
Ocn	Rat	GCAGACCTAGCAGACACCAT	TTGGACATGAAGGCTTTGTCA

Abbreviations: BMSC: Bone marrow mesenchymal stem cell; qRT-PCR: Quantitative reverse transcription polymerase chain reaction.

evaluated by immunofluorescence staining. After 3 days of co-culture, HUVECs were fixed with 4% paraformaldehyde. Following permeabilization with 0.1% Triton X-100 and blocking with 1% BSA, the cells were incubated overnight at 4 °C with primary antibodies against CD31 and VEGF, respectively. Subsequently, the cells were incubated with the corresponding fluorophore-conjugated secondary antibodies for 1 h at room temperature in the dark, and the nuclei were counterstained with DAPI. Images were acquired using a fluorescence microscope, and the relative fluorescence intensity of each group was quantitatively analyzed using ImageJ software.

2.9. Surgical procedures

All animal experimental procedures were reviewed and approved by the Animal Ethics Committee of Nanjing University of Chinese Medicine (202504A084). A total of 15 SD rats were used in this study. Eight-week-old female SD rats were purchased and acclimatized for one week before surgery. To establish the osteoporotic model, the rats were subjected to general anesthesia via isoflurane inhalation. Under sterile conditions, an osteoporosis model was established by bilateral ovariectomy through a dorsal incision. Twelve weeks post-operation, after confirming the successful establishment of the model, the rats underwent cranial bone defect surgery. The skin was incised along the sagittal midline of the skull, and the periosteum was bluntly dissected to expose the cranium. A critical-sized bone defect was created by slowly drilling the center of the bilateral parietal bones using a trephine with an outer diameter of 5 mm (physiological saline was continuously dripped during drilling to prevent thermal injury).

The rats were randomly divided into three experimental groups (n = 5): the α-TCP group, the α-TCP/ZnO group, and the α-TCP/ZnO/CGA–Eu group. The sterilized scaffolds of each group were implanted into the bone defects. The wounds were rinsed with physiological saline and sutured layer by layer. After surgery, all animals were monitored for survival, wound healing, feeding behavior, activity, body weight, and signs of local infection or inflammation until the scheduled endpoint. All rats were housed under standard conditions and euthanized at 12 weeks post-implantation. The entire cranial specimens containing the implants and surrounding tissues were harvested and immediately fixed in 4% paraformaldehyde for subsequent micro-computed tomography (CT) and histological evaluations.

2.10. Micro-computed tomography and histological evaluation

The fixed cranial specimens were scanned and reconstructed using a high-resolution micro-CT scanning system (SkyScan 1276, Bruker Corporation, Germany). For quantitative analysis, a cylindrical volume of interest with a diameter of 5 mm, corresponding to the original defect dimensions, was defined coaxially with the defect region. The following bone histomorphometric parameters were quantitatively extracted and analyzed within this volume of interest: bone volume fraction (bone volume [BV]/total volume [TV]), trabecular number (Tb.N), trabecular thickness (Tb.Th), and trabecular separation (Tb.Sp).

Following the micro-CT scan, all cranial specimens were decalcified in 10% ethylenediaminetetraacetic acid. The completely decalcified samples were then dehydrated through a graded ethanol series, cleared in xylene, embedded in paraffin, and cut into 5 μm-thick coronal sections. H&E staining was performed to observe the overall bone repair. Masson's trichrome staining was conducted to specifically observe the deposition and maturity of newly formed collagen fibers. Furthermore, to assess *in vivo* expression of osteogenic and angiogenic-related proteins, the sections were incubated with primary antibodies against RUNX2 and CD31 for immunohistochemical staining. All stained sections were photographed under an optical microscope (ZEISS Axio

Table 2. Primer sequences used for qRT-PCR analysis of HUVEC angiogenesis

Genes	Species	Forward primer	Reverse primer
GAPDH	Human	AATGGGCAGCCGTTAGGAAA	GCCCAATACGACCAAATCAGAG
VEGF	Human	TGCATTGGAGCCTTGCCTTG	AGGGTCTCGATTGGATGGCA
CD31	Human	AACGGAAGGCTCCCTTGATG	TAAGAACCGGCAGCTTAGCC
HIF1A	Human	GAACGTCGAAAAGAAAAGTCTCG	CCTTATCAAGATGCGAACTCACA

Abbreviations: HUVEC: Human umbilical vein endothelial cell; qRT-PCR: Quantitative reverse transcription polymerase chain reaction.

Imager 2, Carl Zeiss Microscopy GmbH, Germany). For semi-quantitative analysis using ImageJ, the entire 5-mm defect area in the coronal plane was defined as the region of interest, and three sections from comparable anatomical levels were analyzed per sample. Immunohistochemical quantification, including RUNX2-positive area and CD31-positive microvessel-like structures (number and area), was normalized to the α-TCP group set as the baseline of 1.

2.11. Statistical analysis

All experimental data are presented as the mean ± standard deviation (SD). Statistical analysis and the generation of quantitative graphs were performed using GraphPad Prism 10 software (GraphPad Software, USA). Comparisons between two groups were performed using Student's *t*-test, while comparisons among multiple groups were conducted using a one-way analysis of variance (ANOVA) combined with Tukey's *post hoc* test. The significance level was set at 95%, meaning a $p < 0.05$ was considered statistically significant.

3. Results

3.1. Successful synthesis and antioxidant characterization of chlorogenic acid–europium nanoparticles

We successfully synthesized CGA–Eu nanoparticles through coordination-driven self-assembly (Figure 2A). TEM and SEM imaging (Figure 2B and 2C) revealed that the CGA–Eu nanoparticles possessed a regular and well-dispersed microscopic morphology. DLS analysis confirmed a uniform size distribution with an average hydrodynamic diameter of approximately 189 nm (Figure 2D). The radical scavenging ability of the nanoparticles was evaluated via DPPH and ABTS assays. As demonstrated in Figure 2E and 2F, the nanoparticles efficiently scavenged both radicals, with the scavenging efficiency increasing in a clear time- and concentration-dependent trend. Having successfully synthesized and validated the potent antioxidant capacity of the CGA–Eu nanoparticles, we next integrated them into an inorganic matrix to construct the structural foundation for our functional scaffolds.

3.2. Preparation and physicochemical properties of 3D-printed scaffolds

Three types of composite scaffolds (α-TCP, α-TCP/ZnO, and α-TCP/ZnO/CGA–Eu) were fabricated using 3D printing technology (Figure 2G). Rheological analysis (Figure 2H and 2I) demonstrated that the viscosity of the bioink rapidly decreased with increasing shear rate, exhibiting excellent shear-thinning behavior. When the shear stress was removed, the viscosity recovered quickly, demonstrating its good printability and shape-retention capacity. Macroscopic observations and SEM imaging (Figure 2J and 2K) showed that all three groups of scaffolds possessed a well-defined porous structure, which is conducive to nutrient transport and cell growth. EDS mapping revealed a uniform distribution of C, P, Ca, Zn, and Eu elements within the scaffolds (Figure 2L).

Mechanical property tests (Figure 2M) indicated that the compressive strengths of the α-TCP, α-TCP/ZnO, and α-TCP/ZnO/CGA–Eu scaffolds were 22.52 ± 0.89 MPa, 24.01 ± 1.70 MPa, and 25.56 ± 1.32 MPa, respectively. The compressive strengths of all scaffolds were within the appropriate range for cancellous bone repair. During the eight-week *in vitro* degradation period, all groups of scaffolds exhibited varying degrees of degradation, among which the α-TCP/ZnO/CGA–Eu group showed the fastest degradation rate (Figure 2N). In the *in vitro* degradation assay, the early degradation products of pure α-TCP were slightly acidic; the incorporation of ZnO successfully buffered this acidification (Figure 2O). In addition, the *in vitro* release assay demonstrated a steady and sustained release of Zn^{2+}, Eu^{3+}, and CGA from the composite scaffolds (Figure 2P and 2Q). To evaluate the stimuli-responsive release behavior of the scaffolds, we compared the cumulative release of CGA, Eu^{3+}, and Zn^{2+} in normal PBS and in a simulated osteoporotic microenvironment. Under these conditions, the α-TCP/ZnO/CGA–Eu scaffold released CGA and Eu^{3+} at 16.50 ± 0.48 μg/mL and 8.27 ± 0.65 μg/mL, respectively, higher than 13.96 ± 0.31 μg/mL and 6.17 ± 0.33 μg/mL in normal PBS. For Zn^{2+}, the release increased from 10.59 ± 0.53 μg/mL to 13.33 ± 0.45 μg/mL in the α-TCP/ZnO group and from 10.84 ± 0.42 μg/mL to 13.10 ± 0.37 μg/mL in the α-TCP/ZnO/CGA–Eu group (Figure 2P and 2Q). These results indicate that the simulated osteoporotic condition significantly promotes the release of all components.

3.3. *In vitro* biocompatibility and antioxidative stress evaluation of the scaffolds

An initial assessment of scaffold biocompatibility was conducted via cytoskeleton staining (Figure 3A). Compared to the control, BMSCs treated with all scaffolds exhibited a markedly extended morphology. Quantitative analysis (Figure 3B) indicated that the cell spreading area of the α-TCP and α-TCP/ZnO groups increased sequentially, while the α-TCP/ZnO/CGA–Eu group exhibited the largest cell spreading area. The LDH release assay (Figure 3C) showed no significant difference among all scaffold groups and the control group, indicating that the scaffolds caused no obvious cytotoxicity or cell membrane damage. CCK-8 assay results (Figure 3D) revealed that, compared with the control group, the α-TCP group showed no

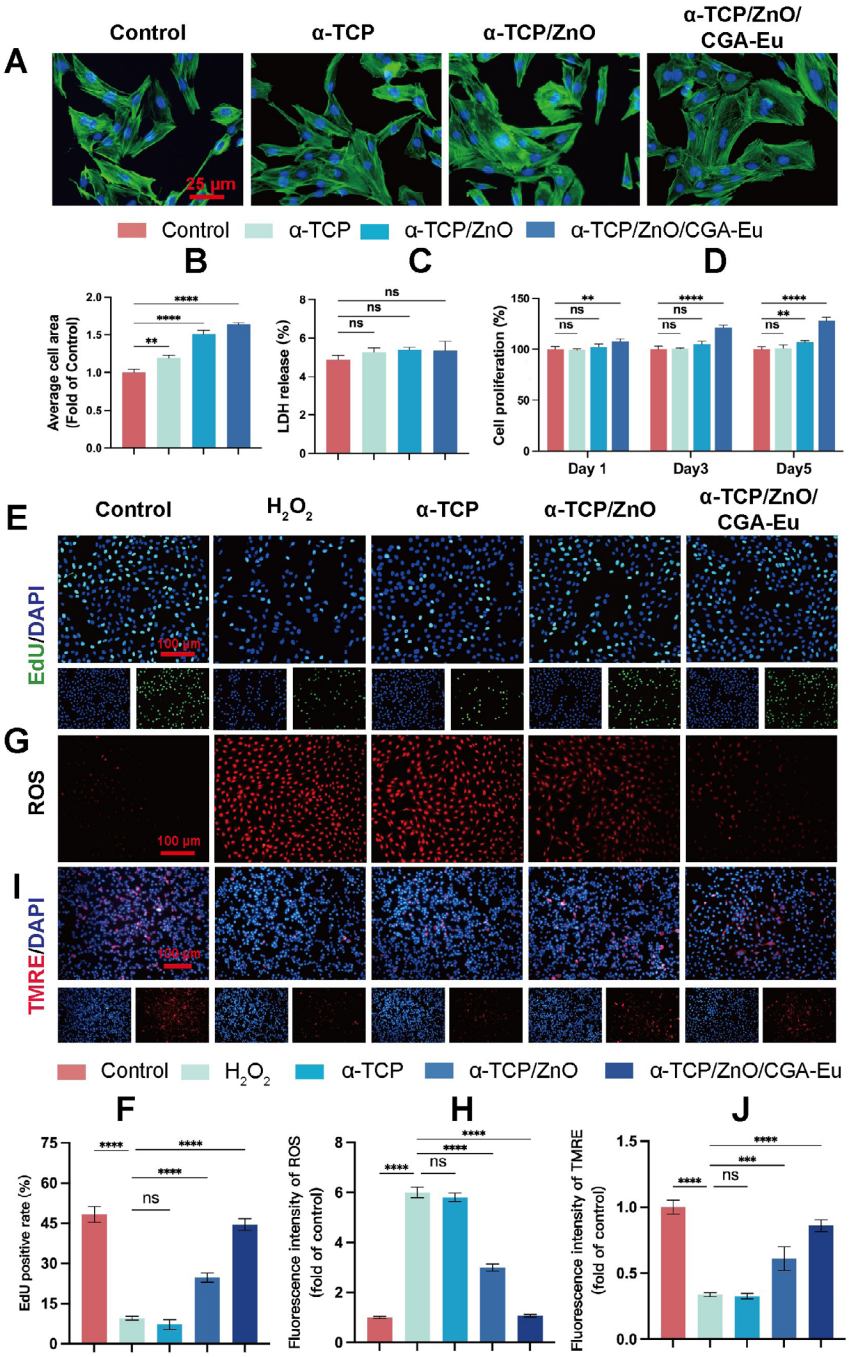

Figure 3. Biocompatibility of the scaffolds. (A) Cytoskeleton fluorescence staining (scale bars: 25 μm; magnifications: 400×) and (B) quantitative analysis of BMSCs spreading area. (C) LDH release rate of BMSCs. (D) CCK-8 cell proliferation assay at days 1, 3, and 5. (E) Representative images of EdU staining (scale bars: 100 μm; magnifications: 100×) and (F) the percentage of proliferative cells. (G) Intracellular ROS fluorescence staining (scale bars: 100 μm; magnifications: 100×) and (H) relative intensity quantification. (I) TMRE fluorescence staining for evaluating mitochondrial membrane potential (scale bars: 100 μm; magnifications: 100×) and (J) quantitative analysis of relative TMRE fluorescence intensity. Notes: ** $p < 0.01$, *** $p < 0.001$, **** $p < 0.0001$, and ns: No significance. $n = 3$.

Abbreviations: α-TCP: α-tricalcium phosphate; BMSC: Bone marrow mesenchymal stem cell; CCK: Cell-counting kit; CGA–Eu: Chlorogenic acid–europium; DAPI: 4',6-diamidino-2-phenylindole; EdU: 5-ethynyl-2'-deoxyuridine; LDH: Lactate dehydrogenase; ROS: Reactive oxygen species; TMRE: Tetramethylrhodamine ethyl ester perchlorate; ZnO: Zinc oxide.

significant difference at any time point. The α-TCP/ZnO group only promoted cell proliferation on day 5, whereas the α-TCP/ZnO/CGA–Eu group significantly promoted cell proliferation on days 1, 3, and 5.

We subsequently investigated the cytoprotective effect of the scaffolds under an oxidative stress microenvironment. Accordingly, BMSCs were treated with H_2O_2 to induce high intracellular ROS levels and proliferation impairment. The EdU proliferation assay (Figure 3E and 3F) indicated that H_2O_2 treatment significantly inhibited cell proliferation. The pure α-TCP group failed to rescue this proliferation impairment, and the α-TCP/ZnO group only achieved partial recovery. In contrast, the α-TCP/ZnO/CGA–Eu group maximally reversed the oxidative stress-induced proliferation inhibition, restoring the cell proliferation rate to a level close to that of the normal control group. Meanwhile, ROS fluorescence staining (Figure 3G and 3H) showed that intracellular ROS levels increased sharply after H_2O_2 stimulation. The pure α-TCP scaffold did not effectively reduce ROS levels, and the α-TCP/ZnO scaffold only scavenged a limited portion of ROS. In contrast, the α-TCP/ZnO/CGA–Eu scaffold efficiently scavenged ROS to a level approaching that of the normal control group. TMRE staining results (Figure 3I and 3J) showed that H_2O_2 exposure induced severe mitochondrial depolarization, evidenced by a drastic decrease in red fluorescence. The pure α-TCP scaffold failed to prevent this depolarization, whereas the α-TCP/ZnO scaffold partially restored the membrane potential. Notably, the α-TCP/ZnO/CGA–Eu scaffold exhibited the highest protective efficacy, restoring the TMRE fluorescence intensity to a level nearly equivalent to that of the normal control group. This preservation of mitochondrial integrity perfectly corroborates the rescued cell proliferation and ROS scavenging capability of the composite scaffold.

3.4. Scaffolds promote osteogenic differentiation of bone marrow mesenchymal stem cells under an oxidative stress microenvironment

We sought to determine the protective and promotive effects of the scaffolds on BMSC osteogenic differentiation under oxidative stress. Therefore, SA-β-gal staining was initially performed. Figure 4A and 4B show that H_2O_2 treatment induced cellular senescence. The pure α-TCP scaffold failed to alleviate this phenomenon; the α-TCP/ZnO scaffold significantly decreased the proportion of senescent cells, whereas the α-TCP/ZnO/CGA–Eu scaffold minimized cellular senescence.

At the osteogenic phenotype level, H_2O_2 severely inhibited early ALP activity (Figure 4C and 4F) and late-stage extracellular matrix mineralization (ARS and Von Kossa staining, Figure 4D–F). The pure α-TCP and α-TCP/ZnO scaffolds mildly and moderately restored osteogenic differentiation, respectively. In contrast, the α-TCP/ZnO/CGA–Eu group demonstrated the most potent osteogenic efficacy, with its ALP activity and mineralized area reaching the highest levels, even significantly exceeding the baseline level of the normal control group.

At the molecular expression level, immunofluorescence staining and quantitative analysis (Figure 4G–I) revealed that H_2O_2 significantly downregulated the expression of key osteogenic proteins OCN and RUNX2. The α-TCP and α-TCP/ZnO groups facilitated a stepwise recovery in the expression of these two proteins, whereas the α-TCP/ZnO/CGA–Eu group achieved the highest fluorescence intensity. Consistently, qRT-PCR results (Figure 4J) further confirmed that the α-TCP/ZnO/CGA–Eu scaffold maximally upregulated the mRNA expression of osteogenesis-related genes (*Runx2*, *Ocn*, and *Alp*), comprehensively reversing the osteogenic inhibition induced by oxidative stress.

3.5. Scaffolds promote the angiogenic differentiation of human umbilical vein endothelial cells under an oxidative stress microenvironment

Given that successful bone regeneration is strictly coupled with angiogenesis, we further explored the protective and pro-angiogenic effects of the composite scaffolds on vascular endothelial cells under oxidative stress conditions. Therefore, the proliferation capacity of HUVECs was first assessed via an EdU assay (Figure 5A and 5B). The results showed that H_2O_2 treatment significantly inhibited cell proliferation. Treatment with the pure α-TCP scaffold failed to alleviate the H_2O_2-induced proliferation inhibition, and the α-TCP/ZnO scaffold only partially restored proliferative activity. In contrast, the α-TCP/ZnO/CGA–Eu scaffold effectively reversed the H_2O_2-induced proliferation inhibition, restoring the cell proliferation rate to a level approaching that of the normal control group.

In the *in vitro* angiogenesis evaluation, the tube formation assay (Figure 5C) and the quantification of total tube length (Figure 5D) demonstrated that H_2O_2 treatment severely disrupted the formation of capillary-like networks. The α-TCP group failed to improve the tube formation capacity, and the α-TCP/ZnO group facilitated a moderate recovery. In contrast, the α-TCP/ZnO/CGA–Eu group promoted the formation of the densest and most continuous capillary-like networks by HUVECs, with the total tube length fully restored to the normal control level.

Immunofluorescence staining and quantitative analysis (Figure 5E–G) demonstrated that the α-TCP/ZnO/CGA–Eu group most effectively reversed the H_2O_2-

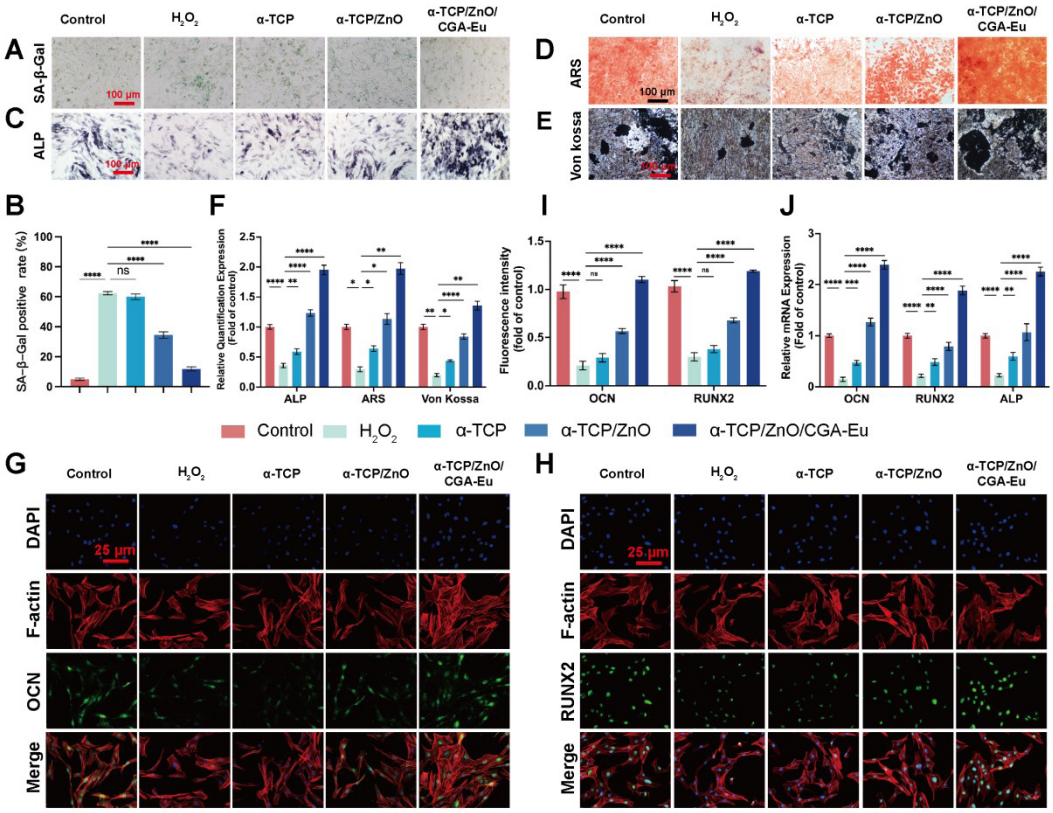

Figure 4. Effects of scaffolds on the osteogenic differentiation of BMSCs. (A) SA-β-gal staining (scale bar: 100 μm; magnification: 100×) and (B) quantification of the SA-β-gal positive rate. (C) ALP staining, (D) ARS staining, and (E) Von Kossa staining. Scale bars: 100 μm; magnifications: 100×. (F) Quantitative analysis of ALP activity at day 7, ARS staining at day 21, and mineralized area at day 21. (G, H) Immunofluorescence staining (scale bars: 25 μm; magnifications: 400×) and (I) corresponding fluorescence intensity quantification of OCN and RUNX2. (J) Relative mRNA expression of *Ocn*, *Runx2*, and *Alp*. Notes: * $p < 0.05$, ** $p < 0.01$, *** $p < 0.001$, **** $p < 0.0001$, and ns: No significance. $n = 3$.

Abbreviations: α-TCP: α-tricalcium phosphate; ALP: Alkaline phosphatase; ARS: Alizarin red S; BMSC: Bone marrow mesenchymal stem cell; CGA–Eu: Chlorogenic acid–europium; DAPI: 4',6-diamidino-2-phenylindole; OCN: Osteocalcin; RUNX2: Runt-related transcription factor 2; SA-β-gal: Senescence-associated β-galactosidase; ZnO: Zinc oxide.

induced inhibition of CD31 and VEGF protein expression, exhibiting superior pro-angiogenic potential. Consistent with these protein-level findings, qRT-PCR results (Figure 5H) revealed that H_2O_2 significantly downregulated the mRNA expression levels of *HIF1A*, *VEGF*, and *CD31*. The pure α-TCP group had no significant effect on rescuing gene expression, and the α-TCP/ZnO group achieved only partial upregulation. In contrast, the α-TCP/ZnO/CGA–Eu group significantly activated transcription of the aforementioned genes, with mRNA expression levels exceeding those of the normal control group.

3.6. Scaffolds promote the regenerative repair of osteoporotic bone defects *in vivo*

To translate our *in vitro* findings into a physiological context, we established an OVX rat cranial bone defect model and implanted the scaffolds of each group. During the 12-week postoperative observation period, all animals survived to the scheduled endpoint, with no wound infections, obvious exudate, abnormal feeding behavior, activity impairment, or marked body-weight loss. Micro-CT and 3D reconstruction images at 12 weeks post-operation (Figure 6A) illustrated the scaffold degradation and the spatial distribution of newly formed bone. All three groups of scaffolds exhibited varying degrees of degradation. Notably, the α-TCP/ZnO/CGA–Eu scaffold degraded the fastest, a finding consistent with our *in vitro* degradation results. Regarding bone repair, only a sparse amount of new bone formation was observed at the defect margins and around the scaffold in the pure α-TCP group. This amount increased in the α-TCP/ZnO group. In striking contrast, abundant and continuous newly formed bone tissue was visible within the scaffold pores and surrounding areas in the α-TCP/ZnO/CGA–Eu group.

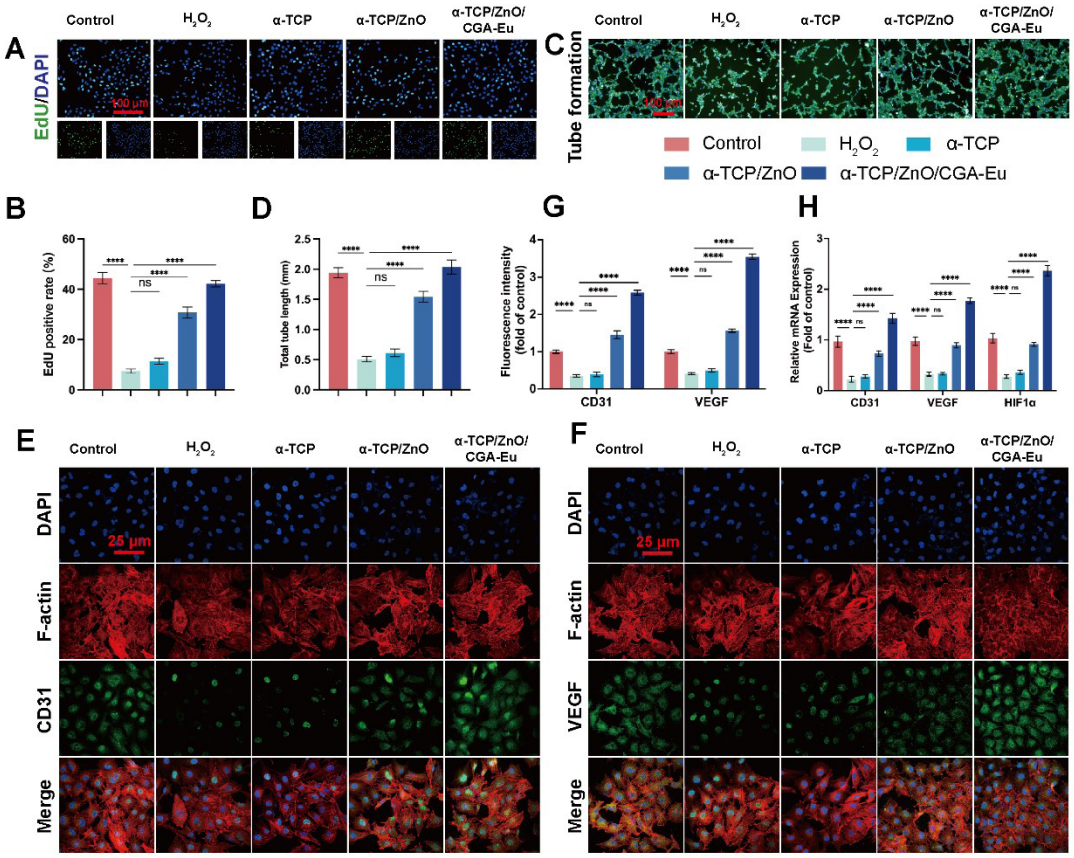

Figure 5. Effects of scaffolds on the angiogenic differentiation of HUVECs. (A) EdU staining (scale bar: 100 μm; magnification: 100×) and (B) positive rate. (C) Tube formation assay (scale bar: 100 μm; magnification: 100×) and (D) quantification of total tube length. (E, F) Immunofluorescence (scale bars: 25 μm; magnifications: 400×) and (G) intensity quantification of CD31 and VEGF. (H) Relative mRNA expression of *CD31*, *VEGF*, and *HIF1A*. Notes: **** $p < 0.0001$, and ns: No significance. $n = 3$.

Abbreviations: α-TCP: α-tricalcium phosphate; CGA–Eu: Chlorogenic acid–europium; DAPI: 4',6-diamidino-2-phenylindole; EdU: 5-ethynyl-2'-deoxyuridine; HUVEC: Human umbilical vein endothelial cell; VEGF: Vascular endothelial growth factor; ZnO: Zinc oxide.

Bone microstructural parameters (Figure 6B–E) further confirmed these observations: the BV/TV, Tb.N, and Tb.Th increased sequentially among the α-TCP, α-TCP/ZnO, and α-TCP/ZnO/CGA–Eu groups, while the Tb.Sp decreased sequentially. This indicated that the α-TCP/ZnO/CGA–Eu scaffold markedly promoted local bone mass accumulation.

The H&E staining results (Figure 6F) revealed that continuous newly formed tissue was generated in all three groups. However, the bone defect area in the α-TCP group was covered by only a relatively thin layer of tissue. Scaffold degradation in the α-TCP/ZnO/CGA–Eu group was the most pronounced. Its surroundings and interstices were occupied by newly formed tissue, demonstrating a repair effect substantially superior to the other groups. Consistent with the H&E results, Masson's trichrome staining (Figure 6G and 6H) showed that the α-TCP/ZnO/CGA–Eu group achieved the most favorable repair outcome. The defect area was filled with abundant dense, newly formed collagen fibers (stained dark blue in Masson's staining) and new bone tissue, with the scaffold degradation matching the tissue ingrowth process. In contrast, the defect area in the pure α-TCP group was predominantly occupied by fibrous connective tissue. No evident tissue necrosis, severe inflammatory cell infiltration, or thick fibrous capsule formation was observed around the implanted scaffolds at 12 weeks, indicating acceptable local tissue compatibility.

Furthermore, to validate the *in vivo* osteogenic and angiogenic activities at the molecular level, immunohistochemical staining for RUNX2 and CD31 was performed (Figure 6I–M). Consistent with the histological findings, the areas of positive expression for both RUNX2

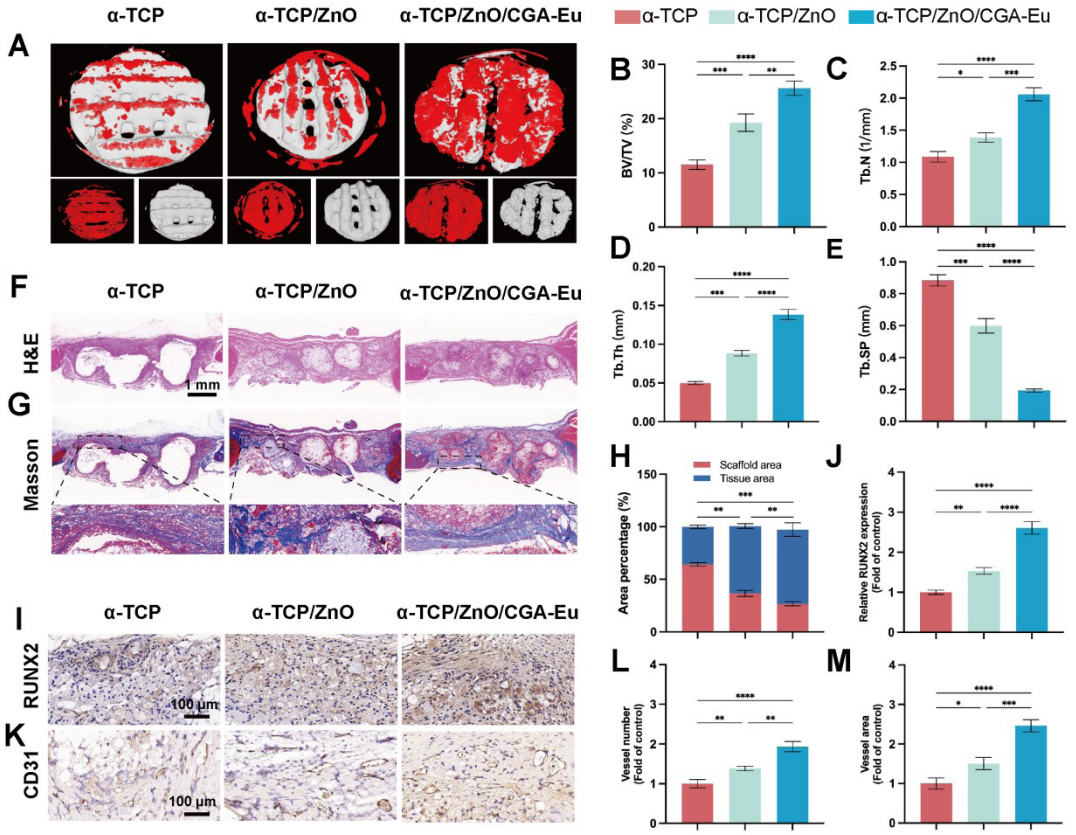

Figure 6. *In vivo* evaluation of bone regeneration in osteoporotic defects. (A) Micro-computed tomography reconstruction of bone and scaffolds within the defect area. Bone microstructural parameters including (B) BV/TV, (C) Tb.N, (D) Tb.Th, and (E) Tb.Sp. (F) H&E and (G) Masson's trichrome staining of the regenerated bone tissue. Scale bars: 1 mm; magnification: 4×. (H) Quantitative analysis of the area percentage for the scaffold and tissue. (I) RUNX2 immunohistochemical staining images (scale bar: 100 μm; magnification: 10×) and corresponding (J) quantitative analysis of relative expression. (K) CD31 immunohistochemical staining images. Scale bar: 100 μm; magnification: 10×. Quantitative analysis of (L) vascular number and (M) vessel area. Notes: * $p < 0.05$, ** $p < 0.01$, *** $p < 0.001$, **** $p < 0.0001$. $n = 5$.

Abbreviations: α-TCP: α-tricalcium phosphate; BV/TV: Bone volume/Total volume; CGA–Eu: Chlorogenic acid–europium; H&E: Hematoxylin and eosin; RUNX2: Runt-related transcription factor 2; Tb.N: Trabecular number; Tb.Sp: Trabecular separation; Tb.Th: Trabecular thickness; ZnO: Zinc oxide.

and CD31 were lowest in the pure α-TCP group and were partially upregulated in the α-TCP/ZnO group. Ultimately, these expressions reached their peak in the α-TCP/ZnO/CGA–Eu group. These results conclusively demonstrated that the composite scaffold accelerates repair of osteoporotic bone defects by synergistically promoting angiogenesis and osteogenesis.

4. Discussion

The repair of osteoporotic bone defects remains a long-standing clinical challenge, primarily because the local microenvironment of osteoporotic defects is characterized by abnormal accumulation of ROS. Such oxidative stress not only inhibits osteogenic differentiation of BMSCs during bone repair and regeneration but also impairs the reconstruction of bone microvascular networks.[5,34,35] As inert filling materials, traditional inorganic bioceramics lack the capability to actively regulate the microenvironment, making it difficult to effectively promote bone tissue regeneration under high oxidative stress conditions. To address this challenge, we constructed a 3D-printed α-TCP/ZnO/CGA–Eu composite scaffold. In this scaffold, ZnO buffered α-TCP degradation-associated acidity and released Zn^{2+}, while CGA–Eu scavenged ROS and provided sustained Eu^{3+}/CGA release. Thus, pH regulation, ROS attenuation, and osteogenic–angiogenic modulation were integrated into a single scaffold. In an OVX rat cranial defect model, it effectively accelerated bone mass accumulation and angiogenesis.

In bone tissue engineering, an ideal scaffold matrix

must simultaneously fulfill the requirements of mechanical support and bioactive molecule loading. 3D printing enables customization according to the location and shape of the bone defect, and allows the creation of interconnected porous structures. By adjusting printing parameters, scaffold degradation can also be controlled, effectively supporting nutrient exchange and providing the necessary space for cell migration and tissue ingrowth.[36] Among available inorganic matrices, α-TCP is particularly well suited for 3D printing because it sets at room temperature via hydration, without the high-temperature sintering (1,100–1,130 °C) that conventional β-TCP ceramics require and that inevitably destroys the structure and function of loaded biomolecules.[12,13] Upon contact with water, α-TCP powder rapidly precipitates into an interwoven network of calcium-deficient hydroxyapatite, making it an ideal matrix for loading bioactive molecules. However, during early hydrolysis and conversion to calcium-deficient hydroxyapatite or hydroxyapatite, pure α-TCP releases acidic byproducts, leading to a decrease in local pH.[9,10,16] This local mildly acidic environment not only exhibits cytotoxicity, thereby inhibiting the early adhesion, proliferation, and osteogenic differentiation of BMSCs, but also favors osteoclast-mediated bone matrix dissolution, resulting in local bone resorption exceeding bone formation.[9,22] Furthermore, local acidification is prone to inducing aseptic inflammatory responses in surrounding tissues, disrupting the physiological balance between osteogenesis and osteoclastogenesis, and ultimately severely hindering bone regeneration and repair under complex pathological conditions, such as osteoporosis.[7] To address this issue, we incorporated alkaline ZnO nanoparticles. The electrochemical reaction of ZnO in physiological fluids continuously releases hydroxide ions, effectively neutralizing the acidic byproducts generated during early α-TCP degradation and thereby maintaining a near-neutral physiological environment.[17,18] Continuous *in vitro* pH monitoring revealed that the ZnO-containing scaffolds effectively neutralized the acidic byproducts released by α-TCP hydrolysis, maintaining a relatively stable pH in the culture system. The restoration of pH in the local microenvironment provided suitable physicochemical conditions for the early adhesion and proliferation of cells. Consistent with this mechanism, biocompatibility results showed that the ZnO-modified scaffolds promoted BMSCs spreading, maintained high cell viability, and accelerated proliferation compared to the pure α-TCP group. By neutralizing the acidic microenvironment, the composite scaffold protected cells from the acidic degradation products, laying the foundation for subsequent bone regeneration.

The matching between the degradation rate of the scaffold and the formation rate of newly formed bone tissue directly dictates the outcome of bone regenerative repair.[13,37] If degradation is too slow, the prolonged retention of the scaffold *in vivo* not only hinders the ingrowth of nascent bone tissue due to spatial occupation but also tends to induce fibrous encapsulation, ultimately interfering with the bone regeneration process.[10] Conversely, if degradation is excessively rapid, the mechanical properties of the material will significantly deteriorate prior to bone regeneration. Consequently, the scaffold cannot effectively withstand local compressive stress, rendering the newly formed tissue susceptible to mechanical collapse or fracture.[38,39] In our composite system, the incorporation of ZnO and CGA–Eu significantly altered the crystallographic features and degradation behavior of α-TCP. The introduced Eu^{3+} and Zn^{2+} occupy the original lattice sites, inducing point defects such as vacancies and interstitials within the crystal, thereby disrupting the intrinsic crystal structure and decreasing crystallinity.[10,31] Consistent with this crystallographic disruption, our *in vitro* degradation profiling demonstrated that the addition of ZnO and CGA–Eu appropriately accelerated the degradation rate of the composite scaffolds. *In vivo* micro-CT and histological evaluations further confirmed that the degradation rate of the scaffold matched the ingrowth of newly formed bone tissue.

High levels of ROS in the osteoporotic microenvironment can directly induce premature senescence or apoptosis in BMSCs, dramatically decreasing their osteogenic differentiation capacity.[40] Consistent with this pathology, our *in vitro* oxidative stress model demonstrated that H_2O_2 exposure triggered severe BMSC senescence and mitochondrial depolarization. To address this critical issue, we introduced CGA. It contains abundant ortho-diphenolic hydroxyl groups, serving as highly efficient electron and hydrogen donors to capture and neutralize intracellular and extracellular free radicals.[23] In addition to directly scavenging generated ROS, CGA can also inhibit ROS generation at the source. Previous studies have proven that CGA downregulates the protein expression levels of intracellular NADPH oxidases (NOXs) and dual oxidase 2 (DUOX2), thereby reducing the production of superoxide anions and mitochondrial ROS.[24,28] Consistent with this dual antioxidant mechanism, cellular assays demonstrated that the CGA–Eu-incorporated scaffolds effectively scavenged intracellular ROS and restored the mitochondrial membrane potential of BMSCs under oxidative stress. However, free natural polyphenols are highly prone to auto-oxidation and hydrolytic inactivation in physiological fluids. Therefore, this study utilized multi-site coordination cross-linking between Eu and the phenolic hydroxyl groups of CGA to self-assemble a

stable MPN. This coordination structure not only shields polyphenol molecules from premature oxidation and hydrolysis but also transforms their previously passive free diffusion into microenvironment-stimuli-responsive release.[26] The metal-phenolic coordination bonds in the MPN exhibit both pH and ROS responsiveness. In the OP microenvironment, free H^+ ions compete with metal ions for binding to the phenolic hydroxyl groups. This competitive protonation, coupled with the severe oxidation triggered by high ROS concentrations, drives the specific disassembly of the coordination complex. This mechanism achieves the long-term, on-demand delivery of CGA and europium, ensuring sustained cytoprotection throughout the early stages of tissue regeneration.[25,41,42]

Building on the ROS-scavenging and cytoprotective effects of CGA–Eu, the scaffold also needs to support osteogenesis and angiogenesis. The continuous release of Zn^{2+} and Eu^{3+} during scaffold degradation further contributed to osteogenic and angiogenic regulation. In terms of promoting osteogenic differentiation, the ionic radius of Eu^{3+} is close to that of Ca^{2+}, and it possesses a higher ionic potential. It can be internalized by BMSCs, significantly upregulating the expression of osteogenic markers, such as ALP, COL-I, and OCN.[29,30,43,44] This mechanism is consistent with our gene- and protein-level findings, in which the composite scaffold markedly reversed the H_2O_2-induced downregulation of RUNX2, ALP, and OCN. Concurrently, Zn^{2+} enters BMSCs through specific receptors (G protein-coupled receptor 39 [GPR39]/zinc-sensing receptor [ZnR]) or ion channels (transient receptor potential melastatin 7 [TRPM7]), activating osteogenesis-related signaling pathways and similarly driving the transcriptional activation of the aforementioned osteogenic genes.[17] Notably, the zinc ion itself is an essential core cofactor for the catalytic activity of ALP and collagenase. It directly participates in the cleavage of phosphate ester bonds, promotes the release of free phosphate ions, and accelerates the mineralization of the extracellular matrix and the deposition of calcium nodules.[18] These enzymatic and biomineralization effects are consistent with the enhanced ALP activity and extensive calcium nodule deposition observed in our *in vitro* osteogenic differentiation assays. The coordination between transcriptional regulation at the gene level and enzymatic catalysis at the protein level significantly enhanced the osteogenic capacity of the composite scaffold. Regarding angiogenesis, Zn^{2+} and Eu^{3+} exhibited complementary regulatory effects. After being recognized by specific receptors on the surface of endothelial cells, Zn^{2+} activates cell proliferation-related signaling pathways, a phenomenon clearly reflected in the restored HUVEC proliferation rates seen in our EdU evaluations.[45] It can also stabilize and activate HIF-1α, driving the upregulated expression of VEGF and CD31.[17] Meanwhile, Eu^{3+} may further support endothelial cell proliferation and migration and promote the secretion of pro-angiogenic factors such as VEGF and fibroblast growth factor, thereby contributing to early capillary formation and lumen remodeling.[29,30,44]

Recent studies have reported effective 3D-printed scaffolds for bone repair using ion-doping or bioactive coating strategies. Qiang *et al.*[46] developed 3D-printed Zn/Mg-doped hydroxyapatite–polycaprolactone scaffolds and showed that Zn/Mg co-doping promoted osteogenesis and angiogenesis in a rat femoral defect model. Chen *et al.*[47] used laser powder bed fusion to fabricate porous Zn–Mg scaffolds with a drug-doped gelatin methacryloyl coating. This coating regulated Zn^{2+} release and corrosion, thereby improving osteogenic and angiogenic performance. These studies mainly enhanced bone repair through ion delivery, drug loading, or structural optimization. In osteoporotic bone defects, osteogenic and angiogenic capacity is already impaired, and the adverse microenvironment, particularly oxidative stress, further compromises cell function. Under such conditions, simply providing osteogenic or angiogenic signals is often insufficient without concurrent regulation of these unfavorable factors. To address this, we designed an α-TCP/ZnO/CGA-Eu composite scaffold. In this design, microenvironmental regulation and pro-osteogenic/angiogenic stimulation are integrated within a single scaffold to further promote the repair of osteoporotic bone defects.

Based on the *in vitro* results, we evaluated the bone tissue regenerative repair efficacy of the scaffolds in an OVX rat cranial defect model. Micro-CT and histological results demonstrated that the scaffolds exhibited degradation behavior that matches the ingrowth of newly formed bone within 12 weeks post-implantation. A dense trabecular network was formed within the scaffold pores and in the surrounding areas, accompanied by abundant microvessel formation. In the face of the complex osteoporotic pathological microenvironment, pure inorganic ceramic scaffolds or materials doped with a single metal ion often exhibit limited repair efficacy. By virtue of the pH- and ROS-responsive sustained-release system constructed by the MPN and the inorganic matrix, the α-TCP/ZnO/CGA–Eu scaffold developed in this study significantly accelerated local bone mass accumulation and coupled angiogenesis under these highly compromised pathological conditions.

While this study has systematically validated the therapeutic efficacy of the composite scaffold, certain limitations remain to be addressed in future investigations. First, the precise molecular targets of the CGA–Eu MPN and the released metal ions in regulating BMSCs and

endothelial cells have not been fully elucidated and require further exploration using approaches such as transcriptomics. Furthermore, *in vivo* bone regeneration in this study was evaluated only in an OVX rat calvarial defect model. Compared with calvarial defect models, femoral condyle or tibial defect models better simulate the bone repair process under load-bearing conditions. Considering that the efficacy of osteoporotic bone repair should be comprehensively assessed at multiple anatomical sites, future studies will include femoral defects and other weight-bearing models to further validate the scaffold's repair performance under mechanical loading.

5. Conclusion

To address the dual inhibition of osteogenesis and angiogenesis caused by excessive ROS accumulation in osteoporotic bone defects, we successfully engineered a 3D-printed α-TCP/ZnO composite scaffold integrated with CGA–Eu MPNs. This system elegantly fulfills the dual demands for structural support and active microenvironment remodeling. Specifically, the incorporation of ZnO neutralized the acidic byproducts generated by α-TCP degradation, ensuring local pH homeostasis. Concurrently, the CGA–Eu network, forming a stable nanostructure through coordination-driven self-assembly, not only endowed the scaffold with robust ROS scavenging capacity but also achieved the stimuli-responsive, sustained release of active components in an oxidative stress microenvironment. *In vitro* evaluations confirmed that this dual-regulation strategy significantly alleviated oxidative stress-induced senescence and restored BMSC proliferation, restoring their osteogenic differentiation capacity. Simultaneously, it protected HUVECs from oxidative damage, thereby promoting potent vascular network formation. *In vivo*, utilizing the OVX rat cranial defect model, the scaffold exhibited a degradation profile perfectly synchronized with the ingrowth of newly formed bone, significantly accelerating local bone mass accumulation and microvascular reconstruction. In conclusion, this study provides a highly promising dual-action therapeutic platform to overcome the pathological barriers to osteoporotic bone regeneration, holding significant translational value for challenging clinical scenarios.

Acknowledgments

None

Funding

This research was supported by the third batch of Jiangsu Province Traditional Chinese Medicine Leading Talent Training Program (Jiangsu Traditional Chinese Medicine Science and Education [2023] No. 17).

Conflict of interest

The authors declare no conflicts of interest.

Author contributions

Conceptualization: Wenjie Zhao, Xinyu Ding, Pengfei Sun, Wen Min, Junwu Wang

Data curation: Xinyu Ding, Shuai Chen, Peng Ma, Yuqing Zhou

Formal analysis: Wenjie Zhao, Shuai Chen, Hao Chen, Yuqing Zhou, Miaochao Qin

Funding acquisition: Wen Min

Investigation: Wenjie Zhao, Jiachen Zhang, Peng Ma, Xinyu Ding, Shuai Chen

Methodology: Shuai Chen, Pengfei Sun, Hao Chen, Miaochao Qin

Project administration: Junwu Wang, Wen Min

Supervision: Wen Min, Junwu Wang

Writing–original draft: Wenjie Zhao, Xinyu Ding, Shuai Chen

Writing–review & editing: Junwu Wang, Wen Min

Ethics approval and consent to participate

All animal experimental procedures were reviewed and approved by the Animal Ethics Committee of Nanjing University of Chinese Medicine (202504A084).

Consent for publication

Not applicable.

Availability of data

The data that support the findings of this study are available on request from the corresponding author.

References

1. Wang W, Zhang X, Zhang L, *et al*. An immunomodulating regenerating hydrogel that rescues the oxidative microenvironment and reverses cell senescence for osteoporotic bone defects. *ACS Nano*. 2025;19(31):28353-28371.

   doi: 10.1021/acsnano.5c06549

2. Sheppard A, Barfield A, Barton S, Dong Y. Understanding reactive oxygen species in bone regeneration: A glance at potential therapeutics and bioengineering applications. *Front Bioeng Biotechnol*. 2022;10:836764.

   doi: 10.3389/fbioe.2022.836764

3. Wu H, Zhang Q, Zhu J, Wu L, Xiao Y, Yang X. Biomaterials targeting senescent cells for bone regeneration: State-of-the-art and future perspectives. *Bioact Mater*. 2025;54:686-714.

doi: 10.1016/j.bioactmat.2025.09.002

4. Li H, Zhang Z, Liu J, Wang H. Antioxidant scaffolds for enhanced bone regeneration: Recent advances and challenges. *Biomed Eng Online*. 2025;24(1):41.

   doi: 10.1186/s12938-025-01370-z

5. Luo J, Li L, Shi W, Xu K, Shen Y, Dai B. Oxidative stress and inflammation: Roles in osteoporosis. *Front Immunol*. 2025;16:1611932.

   doi: 10.3389/fimmu.2025.1611932

6. Saberi A, Kouhjani M, Mohammadi M, Hosta-Rigau L. Novel scaffold platforms for simultaneous induction osteogenesis and angiogenesis in bone tissue engineering: A cutting-edge approach. *J Nanobiotechnol*. 2023;21(1):351.

   doi: 10.1186/s12951-023-02115-7

7. Müller W, Ackermann M, Al-Nawas B, *et al*. Amplified morphogenetic and bone forming activity of amorphous versus crystalline calcium phosphate/polyphosphate. *Acta Biomater*. 2020;118:233-247.

   doi: 10.1016/j.actbio.2020.10.023

8. Tao S, Li X, Wei W, *et al*. Polymeric coating on β-TCP scaffolds provides immobilization of small extracellular vesicles with surface-functionalization and ZEB1-loading for bone defect repair in diabetes mellitus. *Biomaterials*. 2022;283:121465.

   doi: 10.1016/j.biomaterials.2022.121465

9. Carrodeguas R, De Aza S. α-tricalcium phosphate: Synthesis, properties and biomedical applications. *Acta Biomater*. 2011;7(10):3536-3546.

   doi: 10.1016/j.actbio.2011.06.019

10. Tronco M, Cassel J, dos Santos L. α-TCP-based calcium phosphate cements: A critical review. *Acta Biomater*. 2022;151:70-87.

    doi: 10.1016/j.actbio.2022.08.040

11. Liu S, Chen W, Xiao L, *et al*. Robust osteoconductive β-tricalcium phosphate/L-poly(lactic acid) membrane via orientation-strengthening technology. *ACS Biomater Sci Eng*. 2023;9(9):5293-5303.

    doi: 10.1021/acsbiomaterials.3c00617

12. Bohner M, Santoni B, Döbelin N. β-tricalcium phosphate for bone substitution: Synthesis and properties. *Acta Biomater*. 2020;113:23-41.

    doi: 10.1016/j.actbio.2020.06.022

13. Ni X, Feng J, Liang M, *et al*. Enhancing bone repair with β-TCP-based composite scaffolds: A review of design strategies and biological mechanisms. *Orthop Res Rev*. 2025;17:313-340.

    doi: 10.2147/ORR.S525959

14. Wang J, Xia Y, Hao Z, *et al*. A triple-integrated 3D-printed composite scaffold of high-activity peptide-metal ion-bone cement facilitates osteo-vascular regenerative repair of diabetic bone defects. *Adv Funct Mater*. 2025;35(24):2422950.

    doi: 10.1002/adfm.202422950

15. Xia Y, Jing X, Wu X, Zhuang P, Guo X, Dai H. 3D-printed dual-ion chronological release functional platform reconstructs neuro-vascularization network for critical-sized bone defect regeneration. *Chem Eng J*. 2023;465:143015.

    doi: 10.1016/j.cej.2023.143015

16. Safronova T, Selezneva II, Tikhonova S, *et al*. Biocompatibility of biphasic α,β-tricalcium phosphate ceramics in vitro. *Bioact Mater*. 2020;5(2):423-427.

    doi: 10.1016/j.bioactmat.2020.03.007

17. Li P, Dai J, Li Y, *et al*. Zinc based biodegradable metals for bone repair and regeneration: Bioactivity and molecular mechanisms. *Mater Today Bio*. 2024;25:100932.

    doi: 10.1016/j.mtbio.2023.100932

18. Molenda M, Kolmas J. The Role of Zinc in Bone Tissue Health and Regeneration—a Review. *Biol Trace Elem Res*. 2023;201(12):5640-5651.

    doi: 10.1007/s12011-023-03631-1

19. Wen X, Wang J, Pei X, Zhang X. Zinc-based biomaterials for bone repair and regeneration: mechanism and applications. *J Mater Chem B*. 2023;11(48):11405-11425.

    doi: 10.1039/D3TB01874A

20. Chen L, Zhou C, Xie Q, *et al*. Zinc Doped Synthetic Polymer Composites for Bone Regeneration: A Promising Strategy to Repair Bone Defects. *Int J Nanomedicine*. 2025;20:8567-8586.

    doi: 10.2147/IJN.S512994

21. Wang Z, Xiang P, Xu Z, *et al*. The role of magnesium, zinc, and strontium in osteoporotic fracture repair. *Bioengineering (Basel)*. 2025;12(2):201.

    doi: 10.3390/bioengineering12020201

22. Shen J, Zhang S, Zhang J, Wei X, Wang Z, Han B. Osteogenic mechanism of chlorogenic acid and its application in clinical practice. *Front Pharmacol*. 2024;15:1396354.

    doi: 10.3389/fphar.2024.1396354

23. Huang J, Xie M, He L, Song X, Cao T. Chlorogenic acid: A review on its mechanisms of anti-inflammation, disease treatment, and related delivery systems. *Front Pharmacol*. 2023;14:1218015.

    doi: 10.3389/fphar.2023.1218015

24. Nguyen V, Taine E, Meng D, Cui T, Tan W. Chlorogenic acid: A systematic review on the biological functions, mechanistic actions, and therapeutic potentials. *Nutrients*. 2024;16(7):924.

    doi: 10.3390/nu16070924

25. Wang Y, Li Z, Yu R, *et al*. Metal-phenolic network biointerface-mediated cell regulation for bone tissue regeneration. *Mater Today Bio*. 2024;30:101400.

    doi: 10.1016/j.mtbio.2024.101400

26. Lin Z, Liu H, Richardson J, *et al*. Metal–phenolic network composites: From fundamentals to applications. *Chem Soc Rev*. 2024;53(22):10800-10826.

    doi: 10.1039/D3CS00273J

27. Tang Z, Huang Z, Huang Y, *et al*. Nanomedicine's shining armor: Understanding and leveraging the metal-phenolic networks. *J Nanobiotechnol*. 2025;23(1):158.

    doi: 10.1186/s12951-025-03210-7

28. Wu K, Wu X, Guo J, Jiao Y, Zhou C. Facile polyphenol–europium assembly enabled functional poly(l-lactic acid) nanofiber mats with enhanced antioxidation and angiogenesis for accelerated wound healing. *Adv Healthc Mater*. 2021;10(19):2100793.

    doi: 10.1002/adhm.202100793

29. Shi M, Xia L, Chen Z, *et al*. Europium-doped mesoporous silica nanosphere as an immune-modulating osteogenesis/angiogenesis agent. *Biomaterials*. 2017;144:176-187.

    doi: 10.1016/j.biomaterials.2017.08.027

30. Wu L, Yang F, Xue Y, *et al*. The biological functions of europium-containing biomaterials: A systematic review. *Mater Today Bio*. 2023;19:100595.

    doi: 10.1016/j.mtbio.2023.100595

31. Feng S, Peng X, Wu Y, *et al*. Europium-doped 3D dimensional porous calcium phosphate scaffolds as a strategy for facilitating the comprehensive regeneration of bone tissue: In vitro and in vivo. *ACS Biomater Sci Eng*. 2024;10(11):7086-7099.

    doi: 10.1021/acsbiomaterials.4c01067

32. He Z, Sun C, Ma Y, *et al*. Rejuvenating aged bone repair through multihierarchy reactive oxygen species-regulated hydrogel. *Adv Mater*. 2024;36(9):2306552.

    doi: 10.1002/adma.202306552

33. Yao K, Zhang Q, Weng L, *et al*. Cerium-doped, alendronate-loaded, metal–organic framework nanodrug for delayed osteoporosis progress. *ACS Appl Nano Mater*. 2024;7(24):28504-28518.

    doi: 10.1021/acsanm.4c05640

34. Cerqueni G, Scalzone A, Licini C, Gentile P, Mattioli-Belmonte M. Insights into oxidative stress in bone tissue and novel challenges for biomaterials. *Mater Sci Eng C*. 2021;130:112433.

    doi: 10.1016/j.msec.2021.112433

35. Zhang C, Li H, Li J, Hu J, Yang K, Tao L. Oxidative stress: A common pathological state in a high-risk population for osteoporosis. *Biomed Pharmacother*. 2023;163:114834.

    doi: 10.1016/j.biopha.2023.114834

36. Huang D, Li Z, Li G, *et al*. Biomimetic structural design in 3D-printed scaffolds for bone tissue engineering. *Mater Today Bio*. 2025;32:101664.

    doi: 10.1016/j.mtbio.2025.101664

37. Tajvar S, Hadjizadeh A, Samandari SS. Scaffold degradation in bone tissue engineering: An overview. *Int Biodeterior Biodegrad*. 2023;180:105599.

    doi: 10.1016/j.ibiod.2023.105599

38. Zhang J, Jiang Y, Shang Z, *et al*. Biodegradable metals for bone defect repair: A systematic review and meta-analysis based on animal studies. *Bioact Mater*. 2021;6(11):4027-4052.

    doi: 10.1016/j.bioactmat.2021.03.035

39. Cao X, Sun K, Luo J, *et al*. Enhancing osteogenesis and mechanical properties through scaffold design in 3D printed bone substitutes. *ACS Biomater Sci Eng*. 2025;11(2):710-729.

    doi: 10.1021/acsbiomaterials.4c01661

40. Bădilă A, Rădulescu D, Ilie A, Niculescu A, Grumezescu A, Rădulescu A. Bone regeneration and oxidative stress: An updated overview. *Antioxidants (Basel)*. 2022;11(2):318.

    doi: 10.3390/antiox11020318

41. Wei Y, Wei Z, Luo P, Wei W, Liu S. pH-sensitive metal-phenolic network capsules for targeted photodynamic therapy against cancer cells. *Artif Cells Nanomed Biotechnol*. 2018;46(8):1552-1561.

    doi: 10.1080/21691401.2017.1377724

42. Ali A, Javed R, Farhangi S, *et al*. Metal phenolic networks (MPNs)-based pH-sensitive stimulus responsive nanosystems for drug delivery in tumor microenvironment. *J Drug Deliv Sci Technol*. 2023;84:104536.

    doi: 10.1016/j.jddst.2023.104536

43. Wieszczycka K, Staszak K, Woźniak-Budych MJ, Jurga S. Lanthanides and tissue engineering strategies for bone regeneration. *Coord Chem Rev*. 2019;388:248-267.

    doi: 10.1016/j.ccr.2019.03.003

44. Wu C, Xia L, Han P, *et al*. Europium-containing mesoporous bioactive glass scaffolds for stimulating in vitro and in vivo osteogenesis. *ACS Appl Mater Interfaces*. 2016;8(18):11342-11354.

    doi: 10.1021/acsami.6b03100

45. Zhu D, Su Y, Zheng Y, Fu B, Tang L, Qin YX. Zinc regulates vascular endothelial cell activity through zinc-sensing receptor ZnR/GPR39. *Am J Physiol Cell Physiol*. 2018;314(4):C404-C414.

    doi: 10.1152/ajpcell.00279.2017

46. Qiang L, Huang H, Shan J, *et al*. 3D-printed zinc/magnesium-doped hydroxyapatite-polycaprolactone composite scaffolds for angiogenesis and osteogenesis. *Int J Bioprint*. 2024;10(6):4243.

doi: 10.36922/ijb.4243

47. Chen G, Chen C, Dong Z, *et al*. Enhancing degradation behaviour, osteogenic capacity and angiogenic performance of additively manufactured porous Zn-Mg scaffold via a neobavaisoflavone-doped GelMA composite hydrogel coating. *Virtual Phys Prototyping*. 2025;20(1):e2500673.

doi: 10.1080/17452759.2025.2500673